

Vol. 34 • No. 10 • March 4 • 2024

www.afm-journal.de

ADVANCED FUNCTIONAL MATERIALS

WILEY-VCH

Improved Durability of $Ti_3C_2T_z$ at Potentials above the Reversible Hydrogen Electrode by Tantalum Substitution

Bar Favelukis, Sukanta Chakrabartty, Vipin Kumar, Se-Ho Kim, Ayman El-Zoka, Mathias Krämer, Dierk Raabe, Baptiste Gault, Noam Eliaz, Amir Natan, Maxim Sokol, and Brian A. Rosen*


MXenes have gained significant attention, particularly $Ti_3C_2T_z$, as materials with favorable properties for energy storage and conversion applications. The overwhelming majority of electrochemical durability studies are based on durability in the hydrogen evolution window, well below the reversible hydrogen electrode where degradation via electrochemical oxidation is less relevant. Consequently, few strategies have been put forward to protect $Ti_3C_2T_z$ at higher potentials and widen their applicability to electrochemical systems. Here, the electrochemical degradation of pristine $Ti_3C_2T_z$ and tantalum (Ta)-substituted $(Ti_{0.95}Ta_{0.05})_3C_2T_z$ is reported. X-ray photoelectron spectroscopy and electron microscopy revealed that pristine and Ta-doped MXene went through entirely different degradation mechanisms, and that these mechanisms are driven by electrochemical, rather than chemical effects. Density functional theory is used to explain the role of Ta doping with respect to the binding of oxygen and the formation of metal oxide phases. The influence of the degradation mechanism is observed by accelerated stress tests and anode reversal tests on a polymer electrolyte membrane fuel cell. Therefore, the substitution of titanium (Ti) with other oxyphilic metals in $Ti_3C_2T_z$ may be an effective route to improve the durability of the otherwise fragile MXene phase.

1. Introduction

Polymer electrolyte membrane fuel cells (PEMFCs) are a promising electrochemical energy conversion device, and are considered as enablers for efficient and environment-friendly alternative to fossil fuels.^[1] PEMFCs have the capacity to satisfy the ever-increasing global energy demand in a sustainable manner based largely on green fuels. At the core of a PEMFC is an electrocatalyst with high activity and, ideally, stability to provide an uninterrupted energy supply with industrially relevant lifetimes. Traditionally, PEMFC electrodes are platinum (Pt) nanoparticles supported on a microporous carbon substrate. This configuration exhibits high activity and represents the industry standard and benchmark for progress in fuel cell durability. However, parasitic oxidation of the carbon support to CO_2 undermines the lifetime and durability of the fuel cell; therefore, finding suitable replacement supports to improve

B. Favelukis, S. Chakrabartty, N. Eliaz, M. Sokol, B. A. Rosen
Department of Materials Science and Engineering
Tel Aviv University
6997801 Ramat Aviv, Israel
E-mail: barosen@post.tau.ac.il
V. Kumar, A. Natan
Department of Physical Electronics
School of Electrical Engineering
Tel Aviv University
6997801 Ramat Aviv, Israel

V. Kumar, A. Natan
The Sackler Center for Computational Molecular and Materials Science
Tel-Aviv University
6997801 Tel Aviv, Israel
S.-H. Kim
Department of Materials Science and Engineering
Korea University
02841 Seoul, Republic of Korea
S.-H. Kim, A. El-Zoka, M. Krämer, D. Raabe, B. Gault
Max-Planck-Institut für Eisenforschung
Max-Planck-Straße 1, 40237 Düsseldorf, Germany
A. El-Zoka, B. Gault
Department of Materials Science
Royal School of Mines
Imperial College, London
London SW7 2AZ, UK

 The ORCID identification number(s) for the author(s) of this article can be found under <https://doi.org/10.1002/adfm.202309749>

© 2023 The Authors. Advanced Functional Materials published by Wiley-VCH GmbH. This is an open access article under the terms of the Creative Commons Attribution-NonCommercial License, which permits use, distribution and reproduction in any medium, provided the original work is properly cited and is not used for commercial purposes.

DOI: 10.1002/adfm.202309749

the durability of PEMFCs in line with the U.S. Department of Energy's targets for 2025 is highly desirable. Over the last decade, transition metal carbides (TMCs) became popular as an alternative support material to carbon.^[2–4] Unlike carbon, TMCs do not suffer from direct parasitic CO₂ evolution and have been shown by computation to provide particularly strong metal-support interactions with Pt.^[5,6]

In recent years MXenes, a class of 2D transition-metal carbides, gained significant interest in the field of electrocatalysis.^[7,8] MXenes are synthesized by the selective etching of the A-layer in MAX phases, M_{n+1}AX_n, where M represents an early transition metal, A is a group 13 or 14 element, and X represents carbon. The stoichiometry of MXenes is represented as M_{n+1}X_nT_z, where T_z stands for the surface termination group (typically –O, –OH, or –F).^[9,10] Among the discovered MXenes, titanium carbide (Ti₃C₂T_z) has received significant attention due to its high conductivity, high surface area, hydrophilicity, electrochemical activity, and relative ease of synthesis.^[11–14]

However, Ti₃C₂T_z, like many other MXenes, suffers from poor chemical stability which practically hinders its use in electrochemical devices. Ti₃C₂T_z is easily attacked by water and/or oxygen, due to high surface energy and atomic defects.^[15] As a result, it undergoes a rapid structural degradation even in ambient atmospheric conditions. It should be noted that oxidized Ti₃C₂T_z is not yet suitable for electrochemical application as it loses its intrinsic conductivity and ultimately decomposes into TiO₂.^[16–18] In order to improve the stability, several approaches such as antioxidants, and capping agents have been reported.^[15,19]

Furthermore, the electrochemical degradation of Ti₃C₂T_z under applied potential exhibits unique degradation mechanisms which tend to shorten the practical lifetime even further.^[20,21] In this regard, the potential window and pH of the electrolyte are critical factors determining electrochemical stability. According to Göhl et al., the Ti–C bond remains stable at low pH and negative potentials (below reversible hydrogen electrode (RHE)).^[22] This is supported by previous reports describing Ti₃C₂T_z's comparatively stable behavior during hydrogen evolution reaction (HER). Yuan et al. showed durability of Ti₃C₂ nanofibers which could sustain 12 h of continuous electrolysis.^[23] Jiang et al. reported that oxygen-functionalized MXene (Ti₃C₂O_x) had negligible loss in HER performance after 2000 cycles.^[24] In another study, TEM and XPS analysis revealed no change in morphology and chemical bonding in N-doped Ti₃C₂T_z after 30 h of HER chronoamperometry.^[25] Interestingly, Han et al. found the presence of Ti-oxide and hydroxide species on the surface after cycling in XPS analysis. Such species may paradoxically be beneficial and protect MXene from further degradation.^[26]

Although Ti₃C₂T_z-based electrocatalysts have shown stability at negative potentials versus RHE (i.e., during hydrogen electrolysis), their study and application in the positive potential-window remains limited and understudied.^[27] Recently, Nayak et al. studied the electro-oxidation of single Ti₃C₂T_z flakes in acidic electrolyte.^[28] They observed that oxidation of Ti₃C₂T_z started beyond the potential of 0.3 V versus saturated calomel electrode (SCE) and progressed with increasing potential. In addition, they noticed that the controlled oxidation led to improvement in the electrochemical activity of Ti₃C₂T_z whereas the performance declined once Ti₃C₂T_z oxidized completely.

Here, the electrochemical oxidation of Ti₃C₂T_z and Ta-doped (Ta_{0.05}Ti_{0.95})₃C₂T_z in 0.5 M H₂SO₄ at potentials above RHE was investigated. The nominal substitution of 5 at.% Ta for Ti (Ti_{0.95}Ta_{0.05})₃AlC₃ was selected based on previous works by us and others on the improving the durability of transition metal carbides which showed that substitution above 5 at.%, while improving the durability, significantly decreased the activity of the catalyst.^[29,30] The influence of Ta substitution in Ti₃C₂T_z not only improves the corrosion resistance of the MXene, but changes entirely the corrosion mechanism. Impressively, the influence of this novel corrosion mechanism through the influence of Ta was further shown to have a positive effect on the durability PEMFCs which utilized Ti₃C₂T_z as a catalyst support.

2. Results and Discussion

Pristine and Ta-substituted MAX phases were synthesized using the solid-state synthesis technique described in the methods section. Scanning electron microscopy (SEM) coupled with energy dispersive X-ray spectroscopy (EDS) showed that the elemental distribution of Ta in the doped MAX phase was uniform on the micron scale (Figure S1, Supporting Information). X-ray diffraction (XRD) of (Ti_{0.95}Ta_{0.05})₃AlC₃ and Ti₃AlC₃ MAX phases (Figure S2, Supporting Information) showed that the substitution of Ta for Ti caused a shift to lower angles due to the expansion of the unit cell. XRD of the Ti₃C₂T_z and (Ti_{0.95}Ta_{0.05})₃C₂T_z MXene phases are shown in Figure S3 (Supporting Information). Inductively coupled plasma (ICP) analysis of the (Ti_{0.95}Ta_{0.05})₃C₂T_z flakes revealed that the Ta/Ti ratio was 1:17.5, slightly larger than the 1:19.5 ratio expected from the nominal formula. Raman (Figure S4, Supporting Information) showed that Ta-substitution caused no difference the D and G band region, and CHNS analysis revealed that both Ti₃C₂T_z and (Ti_{0.95}Ta_{0.05})₃C₂T_z contained nearly the same amount of carbon (9.85 and 9.30 wt%, respectively). Therefore, the differences in electrochemical performance cannot be attributed to differences in the carbon content or structure between the Ti₃C₂T_z and (Ti_{0.95}Ta_{0.05})₃C₂T_z samples.

Single-flake Ti₃C₂T_z and (Ti_{0.95}Ta_{0.05})₃C₂T_z particles were drop-cast onto a glassy carbon RDE. SEM images in Figure 1a,b showed that MXene flakes were deposited on the electrode in a wide array of orientations and that the electrode, while comprised of single-layer MXene flakes, is effectively multi-layered. Stabilization of the open circuit potential (OCP) required 3 h of contact with the electrolyte. The long stabilization time is attributed to the dissolution of salt residue from the etching process, ion exchange in the termination groups, or osmotic swelling, and is characteristic of MXene phases.^[31]

Figure 1c shows characteristic corrosion curves for 4 μg of Ti₃C₂T_z and (Ti_{0.95}Ta_{0.05})₃C₂T_z. Table 1 summarizes the corrosion metrics, i.e., corrosion potential, passivation potential, corrosion current and passivation current, and their variance over 7 repeated experiments. The corrosion potential increased by 65 ± 15 mV upon the substitution of 5 at.% Ta for Ti. This increase is significant for widening the electrochemical window of the Ti₃C₂T_z-based materials in electrochemical applications, but smaller than the reported impact that the same level of Ta-substitution had on bulk carbides such as Mo₂C (≈120 mV increase with 5 at.% substitution).^[29] Additionally, the average kinetic current decreased by about 20%. While the average

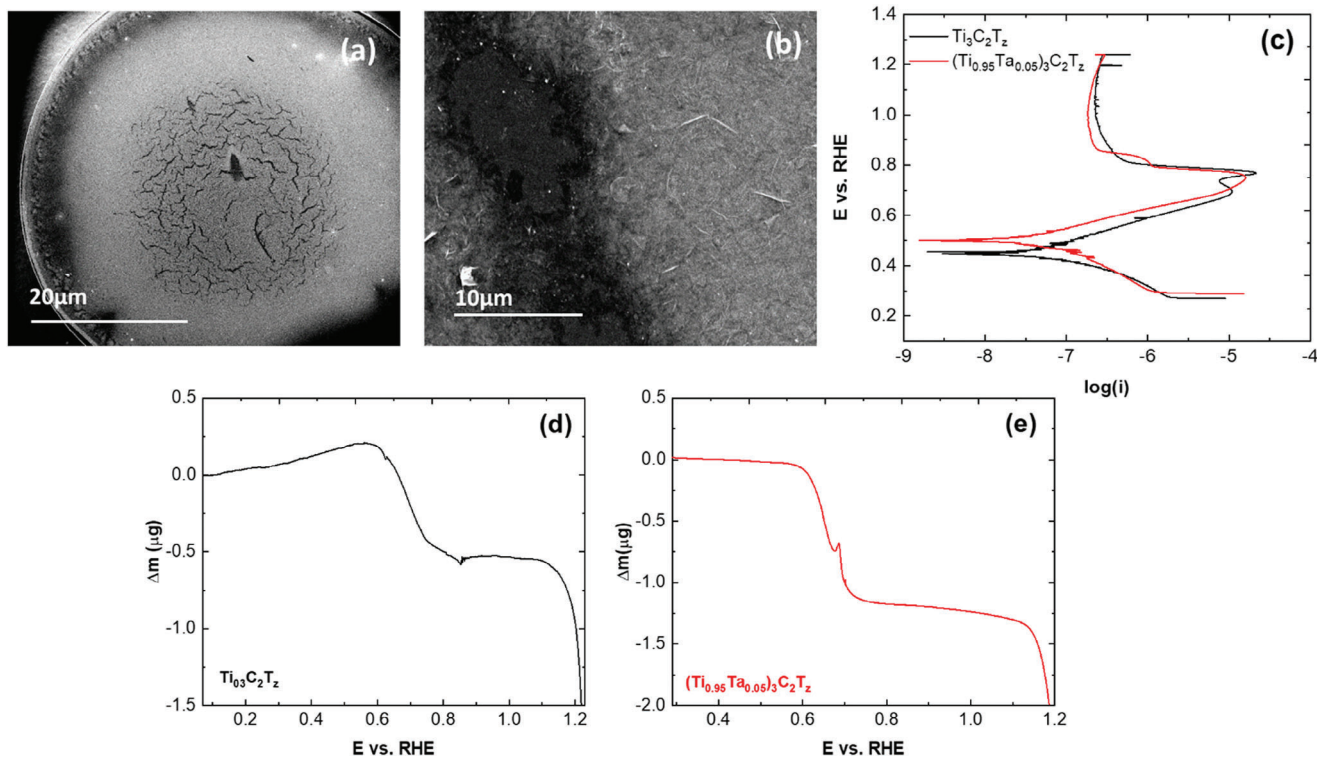


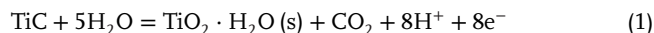
Figure 1. a) Low magnification SEM image showing the dispersion of material on the electrode formed by drop casting $\text{Ti}_3\text{C}_2\text{T}_z$ on an Au disc, b) higher magnification SEM image showing the variation in orientation of the individual flakes because of the drop casting, c) anodic corrosion curves directly comparing $\text{Ti}_3\text{C}_2\text{T}_z$ and $(\text{Ti}_{0.95}\text{Ta}_{0.05})_3\text{C}_2\text{T}_z$ on a glassy carbon RDE. The electrolyte for all experiments was 0.5 M H_2SO_4 with a scan rate of 0.167 mV/s, d) Change in mass as a function of potential for a multilayer drop-casted electrode comprised of $\text{Ti}_3\text{C}_2\text{T}_z$ single-layer flakes on a TiAu electrochemical quartz crystal microbalance (EQCM) electrode, e) Change in mass as a function of potential for a multilayer drop-casted electrode comprised of $(\text{Ti}_{0.95}\text{Ta}_{0.05})_3\text{C}_2\text{T}_z$ single-layer flakes on a TiAu EQCM electrode.

passivation potential increased by 34 mV and the passivation current increased by 34 nA. The variation in these values for the seven different samples suggests that they are not significantly influenced by the addition of Ta.

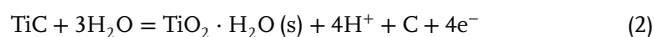
EQCM was used to track the change in mass of the electrode during the same forced anodic polarization of $\text{Ti}_3\text{C}_2\text{T}_z$ (Figure 1d) and $(\text{Ti}_{0.95}\text{Ta}_{0.05})_3\text{C}_2\text{T}_z$ (Figure 1e). The EQCM results showed that both samples exhibited significant mass loss during the initial oxidation step. After the primary passivation potential (E_{pp}), however, the mass stabilized. Importantly, we note that the drop in mass above ≈ 1.1 V versus RHE, along with pitting corrosion, were due to oxidation of the TiAu EQCM electrode and not the MXene flakes. According to Figure 1c, where corrosion testing was done on a glassy carbon rotating disc electrode, the passivation region continues beyond 1.2 V versus RHE. The oxidation process itself is chemically characterized by all the termination

groups being substituted for oxygen, and the oxidation of the $\text{Ti}_3\text{C}_2\text{T}_z$ MXene to TiO_2 and C.^[32] These processes act to passivate the top layer of the electrode and inhibit further corrosion despite the increasing electrochemical potential.

The reactions leading to the observed mass loss are described by the formation of aqueous TiO_2^{2+} , as predicted the Ti-H₂O Pourbaix diagram at pH 1, and additionally CO_2 formation at higher potentials, via the following mechanism:^[33]



or



followed by

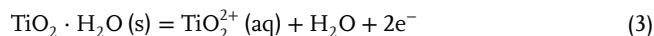


Table 1. Characteristic corrosion metrics derived from forced anodic corrosion curves for $\text{Ti}_3\text{C}_2\text{T}_z$ and $(\text{Ti}_{0.95}\text{Ta}_{0.05})_3\text{C}_2\text{T}_z$.

	E_{corr} [mV vs RHE]	I_{corr} [μA]	E_{pp} [mV vs RHE]	I_{p} [nA]
$\text{Ti}_3\text{C}_2\text{T}_z$	435 ± 14	15.9 ± 5.5	730 ± 28	118 ± 59
$(\text{Ti}_{0.95}\text{Ta}_{0.05})_3\text{C}_2\text{T}_z$	500 ± 17	12.7 ± 8.6	764 ± 17	152 ± 26

X-ray photoemission spectroscopy (XPS) was performed on the $\text{Ti}_3\text{C}_2\text{T}_z$ after forced anodic polarization to 500, 800, 1000, and 1240 mV versus RHE, as shown in Figure 2a. The formation of Ti-O bonds, characterized by peaks in the Ti $2p_{3/2}$ core electron spectrum at 459 and 465 eV, started 0.5M between 500 and 800 mV versus RHE, consistent with the corrosion curves and EQCM data in Figure 1. With increased potential, the Ti-O

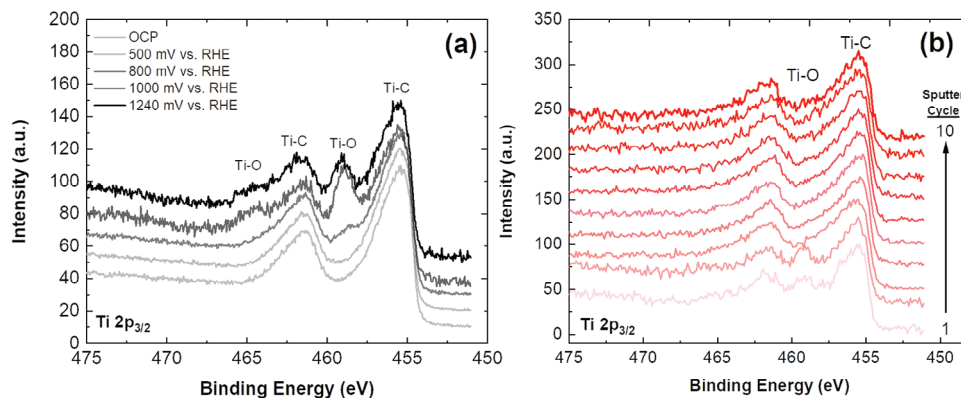


Figure 2. XPS spectra of the a) Ti $2p_{3/2}$ core electron of multilayer drop-casted electrode comprised of $Ti_3C_2T_z$ single-layer flakes as a function of potential on the anodic polarization curve in 0.5 M H_2SO_4 with a scan rate of 0.167 mV/s, b) Ti $2p_{3/2}$ core electron of a multilayer drop-casted electrode comprised of $Ti_3C_2T_z$ single-layer flakes as a function of the sputtering cycle. Larger cycle numbers correspond with larger depth into the thickness of the electrode.

peak became more dominant, but never larger than the Ti–C peak associated with the $Ti_3C_2T_z$ MXene phase. The total atomic oxygen content from XPS went from 16% to 23.5% as the potential was scanned from 500 mV to 800 mV. Despite this, integration of the Ti–C and Ti–O peaks revealed that after forced anodic corrosion to 1240 mV versus RHE, 86% of the surface was Ti–C bonding, compared to 14% Ti–O bonding, and that the relative amount of Ti–O stabilized above 1000 mV owing to passivation.

XPS spectra of the drop-cast $Ti_3C_2T_z$ electrode are plotted in Figure 2b after 1–10 cycles of Ar sputtering. Each sputter cycle carved deeper into the electrode, allowing for XPS characterization as a function of depth into the electrode. The Ti–O peak at 459 eV disappeared after only two cycles, revealing that the oxidation processes described by the EQCM and XPS were limited to the surface, and that MXene single-flakes deeper within the porous electrode were largely protected by MXene flakes closer to the surface. As a result, single $Ti_3C_2T_z$ flakes, which themselves only have three layers, exhibited classical passivation behavior, similar to bulk carbides.

A similar ex situ electrochemical XPS study was carried out using an electrode made from the Ta-substituted MXene, $(Ti_{0.95}Ta_{0.05})_3C_2T_z$. Figure 3 shows the Ti $2p_{3/2}$ and Ta $4f$ core

electron spectra after electrochemical oxidation in 0.5M H_2SO_4 to 800 mV, the potential at which the first Ti–O peaks were seen in the unsubstituted $Ti_3C_2T_z$ MXene (Figure 2a). Interestingly, the Ti–O peak found in the Ti $2p_{3/2}$ spectra of the $Ti_3C_2T_z$ electrode was not observed for the $(Ti_{0.95}Ta_{0.05})_3C_2T_z$ electrode. Instead, the oxygen bond was found only in the Ta $4f$ spectra at ≈ 24 eV. This suggests that the Ta dopant acted to protect the Ti from oxidation by bonding with oxygen first. Indeed, such a change in oxidation mechanism may have a macroscopic impact on the way the Ta-doped MXene degrades relative to pristine $Ti_3C_2T_z$, as will be discussed below.

DFT calculations were used to better rationalize oxygen's preferential bonding with Ta over Ti during the electrochemical oxidation of $(Ti_{0.95}Ta_{0.05})_3C_2T_z$. The first possibility was that the oxygen binds preferentially to Ta rather than Ti on the MXene surface. A second possibility was that the oxygen interacts with the Ti or Ta atoms to form a stable or meta stable TiO or TaO phase, while leaving a vacancy in the original MXene structure.

We modeled the two possibilities for the pristine and Ta doped Ti_3C_2 crystal. The lattice constant and thickness of hexagonal crystal were calculated as 3.07 Å and 3.66 Å; while the bond length of Ti–C is 2.05 Å which agrees well with previous reported values.^[34] Figure 4 shows the geometries of pristine and Ta-doped

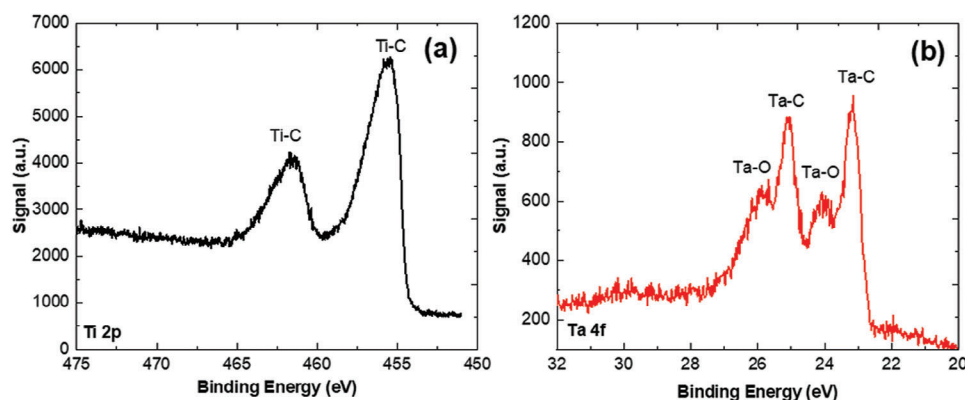


Figure 3. XPS spectra of the a) Ti $2p_{3/2}$ core electron of multilayer drop-cast electrode comprised of $(Ti_{0.95}Ta_{0.05})_3C_2T_z$ single-layer flakes scanned up to 0.8 V versus RHE at 0.167 mV/s in 0.5 M H_2SO_4 , b) Ta $4f$ core electron of the same sample.

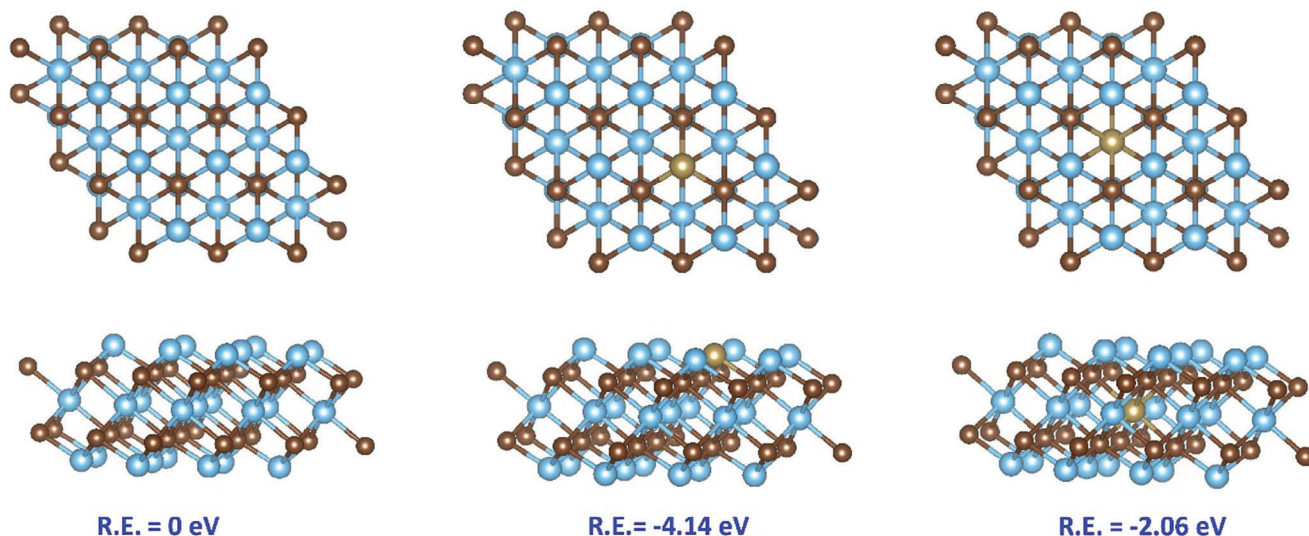


Figure 4. Optimized structures of a) Pristine, b) surface Ta-doped Ti_3C_2 , and c) middle Ta-doped Ti_3C_2 . Carbon atoms are shown in brown, titanium atoms are shown in light blue, the tantalum atom is shown in light brown. The energies shown in blue are the differences in total energy according to Equation 4.

Ti_3C_2 , we calculated the doping energy according to:

$$E(\text{doping}) = E(\text{Ti}_3\text{C}_2 + \text{Ta}) - E(\text{Ti}_3\text{C}_2) - E(\text{Ta}) + E(\text{Ti}) \quad (4)$$

Where $E(\text{Ti})$ and $E(\text{Ta})$ are the energies of the stable phases of Ti and Ta respectively.

For Ta doping and oxygen binding energy calculations, a supercell of $2 \times 2 \times 1$ with 12 Ti atoms and 8 C atoms was generated; for the doped system one Ti atom was replaced with one Ta atom-reaching an effective doping level of 8.33%, only slightly higher than the nominal 5% doping used experimentally. We calculated the vacancy formation energy in Ti_3C_2 when one Ti atom was removed from the surface and found a value of 2.68 eV, which is close to the value of 2.35 eV reported by Siby et al.^[8] Two doping positions in the Ti_3C_2 system were chosen: i) Ti was replaced on the surface layer or ii) Ti was replaced in the middle layer. The doping energies relative to pristine Ti_3C_2 as defined by Equation 7, for Ta-doping on the surface- and middle-layer were -4.14 eV, and -2.06 eV, respectively. Ta-doping on the surface appears more energetically favorable. This contrasts with previous reports by energy loss spectroscopy (EELS) of Ta preferentially doped in the middle layer when Ta substitution for Ti was 38 at%,^[35] as opposed to 8.33% (DFT) and 5 at% (experiment) studied here. The surface-doped system was therefore used for comparative OBE calculations.

Several possible oxygen binding positions were considered, this discussion is found in the supporting information. The adsorption energy of the O atom on the pristine and Ta-doped Ti_3C_2 was observed to be -6.00 eV and -5.40 eV, respectively; this is close to the calculated adsorption energy, of O_2 on the FCC phase of TiC (111) surface, which was found to be -5 eV by Tereshchuk et al.^[36] We note in passing that the DFT calculations do not capture the influence of the MXene termination groups (T_z), which likely convolute the OBE calculation.

The second possibility checked was the formation of a separate TaO or Ta_2O_5 phase.^[37,38] TaO is a meta-stable phase of Ta and

O which is above the convex hull; Ta_2O_5 is a stable phase of Ta and O. We calculated the possible per atom formation energy of TaO and Ta_2O_5 with respect to the Ta-doped MXene in Equation 5 and Equation 6. Similarly, the per atom formation energy of TiO with respect to the Ta-doped and pristine MXene was calculated by Equation 7 and Equation 8:

$$E_F(\text{TaO}) = \frac{1}{2} E(\text{TaO}) + \frac{1}{2} E(\text{Ti}_3\text{C}_2 + \text{Vacancy}) - \frac{1}{2} E(\text{Ti}_3\text{C}_2 + \text{Ta}) - E(\text{O}_2) / 4 \quad (5)$$

$$E_F(\text{Ta}_2\text{O}_5) = \frac{1}{7} E(\text{Ta}_2\text{O}_5) + \frac{2}{7} E(\text{Ti}_3\text{C}_2 + \text{Vacancy}) - \frac{2}{7} E(\text{Ti}_3\text{C}_2 + \text{Ta}) - \frac{5}{7} E(\text{O}_2) / 2 \quad (6)$$

$$E_F(\text{TiO}(\text{Ta})) = \frac{1}{2} E(\text{TiO}) + \frac{1}{2} E(\text{Ti}_3\text{C}_2 + \text{Vacancy}) - \frac{1}{2} E(\text{Ti}_3\text{C}_2 + \text{Ta}) - \frac{E(\text{O}_2)}{4} \quad (7)$$

$$E_F(\text{TiO}) = \frac{1}{2} E(\text{TiO}) + \frac{1}{2} E(\text{Ti}_3\text{C}_2 + \text{Vacancy}) - \frac{1}{2} E(\text{Ti}_3\text{C}_2) - E(\text{O}_2) / 4 \quad (8)$$

First, the binary convex hull formation energies for the meta-stable TaO and stable Ta_2O_5 phases were calculated and found to be -1.22 eV and -3.18 eV respectively, close to the values of -1.24 eV^[39-41] and -3.28 eV,^[41-48] which are reported in the literature.

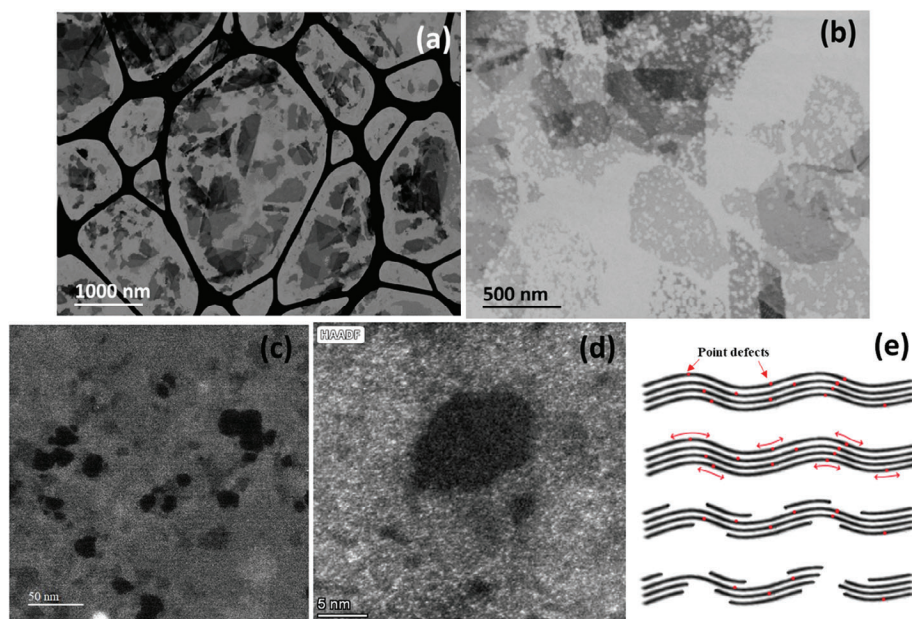


Figure 5. a) Bright-field TEM of $\text{Ti}_3\text{C}_2\text{T}_z$ drop-casted on an Au/lacey carbon TEM grid, b) Bright-field TEM of $(\text{Ti}_{0.95}\text{Ta}_{0.05})_3\text{C}_2\text{T}_z$ drop-casted on an Au/lacey carbon TEM grid, c,d) HAADF of $(\text{Ti}_{0.95}\text{Ta}_{0.05})_3\text{C}_2\text{T}_z$ drop-casted on a Cu/lacey carbon TEM grid, e) schematic representation of MXene “thinning” corrosion mechanism. All images were collected after drop casting pristine MXene onto the TEM grid and scanning to 0.8 V versus RHE at 0.167 mV/s in 0.5 M H_2SO_4 .

The TiO binary convex hull formation energy was calculated by us to be -3.13 eV, close to the value of -2.91 eV reported in the literature.^[41] We next calculated the per-atom formation energies for the TaO and Ta_2O_5 phases relative to MXene and Ta according to Equation 1 and Equation 2 and found values of -0.18 eV and -2.59 eV, respectively. Equation 1–4 were normalized per atom, counting the Ta(Ti) and oxygen atoms in the formed species, this is equivalent to doing a binary convex hull with a shifted reference where the Ta or Ti atom comes from the MXene and not from the metal. For comparison, TiO formation energy relative to the pristine (Equation 7) and the Ta-doped (Equation 4) were also calculated and came to -1.51 eV for both systems. To summarize it is energetically favorable to form a phase of TiO from pristine Ti_3C_2 , which agrees well with the experimental findings.^[49] For the Ta-doped system it was similarly shown that it is energetically favorable to form both TaO and Ta_2O_5 . Importantly, the formation energy of Ta_2O_5 is more favorable than that of TiO, but the formation of TiO was more favorable than TaO. Such a result would suggest that Ta_2O_5 should be the most stable separated phase from Ta oxidation from $(\text{Ti}_{0.95}\text{Ta}_{0.05})_3\text{C}_2\text{T}_z$, and yet, the binding energy of the Ta-O peak found in Figure 3 suggests TaO formation. It is therefore likely that the TaO observed by XPS in Figure 3, while not the most thermodynamically stable, is parallel to the well-known TiO phase formation from the pristine $\text{Ti}_3\text{C}_2\text{T}_z$ MXene.

The impact of Ta-doping on the oxidation mechanism was also studied by transmission electron microscopy. $\text{Ti}_3\text{C}_2\text{T}_z$ and $(\text{Ti}_{0.95}\text{Ta}_{0.05})_3\text{C}_2\text{T}_z$ flakes were both drop-casted onto a lacey carbon TEM grid, which itself was used as the working electrode. The TEM grid, loaded with the MXene sample, was then put through the same forced anodic polarization procedure described in Figure 1, stopping at a potential of 800 mV versus RHE.

Figure 5a,b show bright field TEM images which compare $\text{Ti}_3\text{C}_2\text{T}_z$ and $(\text{Ti}_{0.95}\text{Ta}_{0.05})_3\text{C}_2\text{T}_z$ after polarization, respectively.

The difference in degradation mechanism during electrochemical oxidation for the pristine and Ta-doped MXene is shown in Figure 5a,b. The pristine MXene flakes appeared to have been “shredded” in Figure 5a which has been previously explained by the degradation of MXene initiating from ripples in the basal plane of the MXene.^[49] As a result, the size, and edges of the MXene after electrochemical oxidation no longer resembled sharpness of the original flake. By contrast, the Ta-doped MXene flakes in Figure 5b roughly maintained their original shape during oxidation, and the edges remained sharp and straight. However, a large number of ≈ 5 – 20 nm holes were formed through the basal plane. The preferential oxidation of Ta and subsequent hole formation is believed to better protect the integrity of the flake (particularly at the edges) compared to the “shredding” mechanism, and is likely part of cause for improved performance. Hole formation in the basal plane of MXenes have been previously observed,^[50] but only in strong protonic acids (HCl, HBr, HI)^[51] or exposed to a relatively dilute acid (3 M H_2SO_4) for an extended length of time (48 h).^[52] Here, holes are observed in 0.5 M H_2SO_4 over a comparatively short length of time owing specifically to the electrochemical oxidation of the MXene. Such holes were likely initiated by sacrificial Ta oxidation on the surface as shown by XPS in Figure 3 and explained in part by DFT calculations. We postulate that hole formation is initiated by the selective oxidation of Ta (as illustrated in Figure S5, Supporting Information), resulting in a cation vacancy in the MXene lattice. This vacancy is then susceptible to further attack by oxygen, whereby promoting the formation of a hole despite the mild electrochemical conditions.

Figure 5c,d show high-angle annular dark field (HAADF) TEM images of the holes from a single Ta-doped MXene flake shown

in Figure 5b at higher magnification. The black regions of the HAADF image represent holes. In the region adjacent to the holes are regions that are not black, but also do not have as strong of a HAADF signal (i.e., not as bright) as the undamaged regions of the MXene flake (i.e., dark grey). Since $(\text{Ti}_{0.95}\text{Ta}_{0.05})_3\text{C}_2\text{T}_z$ is a 3-layer MXene, these darker gray regions represent areas where the MXene flake has been reduced to either two or one layer. This suggests that after the initial oxidation of the Ta atom, electrochemical degradation of the MXene first proceeds *laterally* within the same layer, rather than *axially* through the layers. This mechanism is shown schematically in Figure 5e. Here, lateral degradation within the top and bottom surface layers of $\text{Ti}_3\text{C}_2\text{T}_z$ exposes the middle layer to the same mechanism, ultimately forming the hole through all three layers. Such a mechanism has not been previously reported, even for $\text{Ti}_3\text{C}_2\text{T}_z$ perforated with holes via strong and weak acids as cited above. This suggests that the lateral oxidation mechanism may be uniquely part of electrochemical oxidation, rather than chemical oxidation.

Finally, the $\text{Ti}_3\text{C}_2\text{T}_z$ and $(\text{Ti}_{0.95}\text{Ta}_{0.05})_3\text{C}_2\text{T}_z$ flakes were loaded with 40 wt.% Pt (Figure S6, Supporting Information) catalyst support in the anode of a 5 cm² hydrogen-fed proton exchange membrane fuel cell (PEMFC) to test whether the degradation mechanism had an influence on the durability of the fuel cell performance. The fuel cell was exposed to thousands of electrochemical cycles between 0.6–0.9 V (the power generation regime) in an accelerated stress test (AST) meant to test the durability of the catalyst layer. When the MXenes were used as the cathode support (anode catalyst being commercial Pt/C), the degradation proceeded so rapidly that the fuel cell lost most of its performance during the standard break-in procedure for PEMFCs (Figure S7, Supporting Information). It is likely that the high potential of the cathode, together with the high oxygen partial pressure in the cathode compartment created an oxidizing environment which was too harsh to reasonably expect durable performance from the MXene support. When the MXenes were used as an anode support (cathode catalyst being commercial Pt/C) the advantages of the Ta-doping became more apparent. While the anode is the negative electrode in a PEMFC, it still operates at potentials above RHE (typically ≈ 0.1 V) and exposed to an aqueous environment.

Figure 6 shows the result of the AST when the pristine MXene (Figure 6a) and Ta-substituted MXene (Figure 6b) are used as the anode catalyst support. After 20 k cycles, the performance of the PEMFC pristine MXene degraded by about 100 mA cm⁻² at 0.6 V, whereas the PEMFC using the anode with the Ta-substituted MXene showed negligible degradation under the same stress conditions. This experiment was replicated three times. While it is unlikely that the same degradation mechanism observed in Figure 5 is occurring at the PEMFC anode under more mild oxidizing conditions, the MXene in the fuel cell is loaded with 40 wt.% Pt, which in addition to catalyzing the desired H₂ oxidation, has also been shown to catalyze the oxidation of carbides under milder conditions.^[29] Indeed, bright field TEM imaging of Pt/ $(\text{Ti}_{0.95}\text{Ta}_{0.05})_3\text{C}_2\text{T}_z$ recovered from the spent anode catalyst layer after 20 k cycles shows holes in the MXene layer adjacent to Pt particles (Figure S8, Supporting Information). XPS of the same sample (Figure S9, Supporting Information) revealed that 80% of the Ta bonds were with oxygen and the remaining 20% were with carbon.

While the AST protocol described above is typically used for cathode degradation, hydrogen starvation at the anode during such tests can cause the local potential to increase to much higher values. This is evidenced by the difference in performance after the AST despite comparing fuel cells with identical cathodes, and the presence of holes in the $(\text{Ti}_{0.95}\text{Ta}_{0.05})_3\text{C}_2\text{T}_z$ flakes recovered from the anode after the test.

To remove doubt, an additional degradation test was performed specifically to measure the stability of the anode under potential reversal conditions, which more systematically measures anode degradation during fuel starvation. While the full protocol is reported by Ioroi,^[53] in brief, the anode compartment was purged with humidified N₂ and the current density was fixed at 0.2 A cm⁻² causing the cell voltage to drop dramatically (i.e., dramatic increase in anode voltage). This reversal condition was held for 2 h. The cell was then conditioned overnight between 0.3 and 0.5 A cm⁻² using the original H₂ fuel, and the final polarization curve was recorded (“after anode reversal”). Figure 6c,d show the result of the anode reversal experiment for fuel cells containing the $\text{Ti}_3\text{C}_2\text{T}_z$ and $(\text{Ti}_{0.95}\text{Ta}_{0.05})_3\text{C}_2\text{T}_z$ anodes, respectively. The anode reversal test is consistent with the AST and showed that the fuel cell with the $(\text{Ti}_{0.95}\text{Ta}_{0.05})_3\text{C}_2\text{T}_z$ -based anode performed better than the $\text{Ti}_3\text{C}_2\text{T}_z$ -based anode both on an absolute scale, and by comparison to the initial performance.

3. Conclusion

Pristine $\text{Ti}_3\text{C}_2\text{T}_z$ and Ta-substituted $(\text{Ti}_{0.95}\text{Ta}_{0.05})_3\text{C}_2\text{T}_z$ were synthesized and their electrochemical oxidation properties were studied in 0.5 M H₂SO₄ at potentials above the RHE. Ta substitution was found to influence the oxidation mechanism by selectively binding with oxygen prior to lattice Ti. DFT calculations show that it was energetically favorable for TaO to form because of oxygen binding, leaving behind a vacancy in the MXene lattice. Although Ta₂O₅ is predicted to be more stable, the TaO formation mechanism suggested by DFT parallels the TiO formation mechanism in $\text{Ti}_3\text{C}_2\text{T}_z$ reported previously, and by XPS from this study. Vacancy formation is likely the initiation for hole formation, found to be the primary degradation mechanism only in the Ta-substituted MXene. By contrast, the pristine $\text{Ti}_3\text{C}_2\text{T}_z$ showed degradation by decomposition along the ripples typically observed in single-flake $\text{Ti}_3\text{C}_2\text{T}_z$. The Ta-substituted MXene was found to be a more durable support for Pt at the anode of a PEMFC and showed negligible degradation after 20 k accelerated stress test cycles. The Ta-substituted MXene also performed better during an anode reversal test. The substitution of Ta can therefore be considered as a potential strategy for mitigating the effects of electrochemical oxidation in $\text{Ti}_3\text{C}_2\text{T}_z$ at potentials above RHE.

4. Experimental Section

Materials: Titanium (Ti, 99.7%), lithium fluoride (LiF, 99%), and aluminum (Al, 99.7%) powders were received from Strem. Titanium carbide (TiC, 99.5%) and tantalum carbide (TaC, 99.5%) were obtained from Alfa Aesar and Angene, respectively. Hexachloroplatinic acid (H₂PtCl₆ · 6H₂O, >37.5 % Pt basis) was purchased from Merck. Hydrochloric acid (HCl), sulfuric acid (H₂SO₄), ethylene glycol (EG), and isopropanol (IPA) were purchased from Lab-Chem, Israel. SIGRACET GDL 29BC carbon paper, Nafion (20 wt.%), and single-side Pt/C coated Nafion NR-212 electrolyte

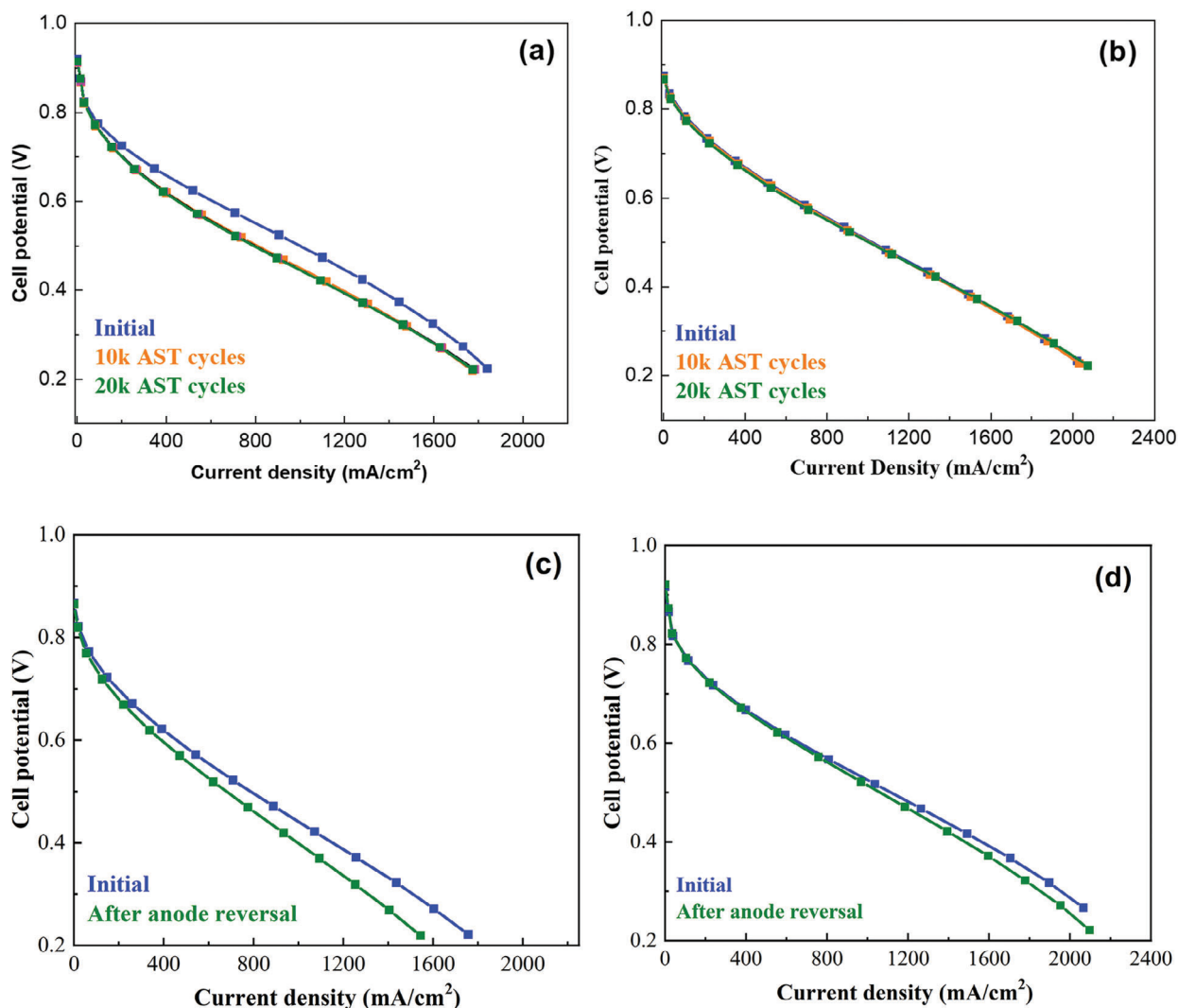


Figure 6. AST curves for a 5 cm² PEM fuel cell cycled between 0.6–0.8 V using commercial Pt/C cathode and a Pt anode supported by a) Ti₃C₂T_z and b) (Ti_{0.95}Ta_{0.05})₃C₂T_z. Polarization curves for a 5 cm² PEM fuel cell with a Pt/C cathode and a Pt anode supported by c) Ti₃C₂T_z and d) (Ti_{0.95}Ta_{0.05})₃C₂T_z before and after anode reversal.

membrane was purchased from Ion-Power. The high purity deionized (DI) water was obtained using Milli-Q system (Millipore, USA).

Synthesis of MAX Ti₃AlC₂ and (Ta_{0.05}Ti_{0.95})₃AlC₂: Ti₃AlC₂ MAX phase was synthesized in the following procedure. Briefly, titanium carbide (TiC), Ti, and Al powders were ball-milled at 1800 rpm for 5 min with a molar ratio of 2:1:1.05. Then, the resulting mixture was pelletized and placed in an alumina crucible for annealing. The temperature of the furnace was kept at 1500 °C for 2 h. The heating rate was 5 °C min⁻¹. During annealing inert atmosphere was maintained by flowing 200 sccm argon (Ar). Thereafter, the annealed sample was ground to fine powder in a ball-mill at 1800 rpm for 5 min.

Synthesis of (Ta_{0.05}Ti_{0.95})₃AlC₂ MAX phase was done in the same procedure as mentioned above only varying the ratio of TiC and TaC. The used molar ratio of TiC, TaC, was 1.85: 0.15.

Synthesis of MXene Ti₃C₂T_z and (Ta_{0.05}Ti_{0.95})₃C₂T_z: Ti₃C₂T_z and (Ta_{0.05}Ti_{0.95})₃C₂T_z were obtained by selective etching of Al-layer of corresponding MAX phases, Ti₃AlC₂ and (Ta_{0.05}Ti_{0.95})₃AlC₂, respectively. Etchant was in situ generated HF. Initially, LiF (0.5 g) was dissolved in 5 mL HCl (10.2 M) in a polyethylene vial. Later, Ti₃AlC₂ or (Ta_{0.05}Ti_{0.95})₃AlC₂ powder (0.5 g) was slowly added to the solution and stirred for 24 h at

35 °C. After etching, the slurry was transferred to a centrifuge tube (50 mL) and the remaining volume was filled by adding DI-water. The product was shaken vigorously and was centrifuged at 5000 rpm for 5 min. The supernatant was decanted, and the washing process was repeated several times until an approximately neutral pH (≥6) was reached. Post-washing, the etched sediment was dispersed in DI water by sonication for 30 min in the presence of ice bath. The resulting black dispersion was then centrifuged at 5000 rpm for 30 min and the colloidal supernatant containing single layer of MXene was collected for future use. To avoid oxidation, the as-obtained MXene solution was purged with Ar and stored in a refrigerator. The yield was 7 mg mL⁻¹, obtained after drying the MXene in a desiccator overnight.

Synthesis of Pt-Ti₃C₂T_z and Pt-(Ta_{0.05}Ti_{0.95})₃C₂T_z: MXenes with 40 wt.% Pt nanoparticles (MXene-Pt) were synthesized by the polyol method. Typically, 2 mL H₂PtCl₆ solution (40 mg mL⁻¹) was added to 45 mg of Ti₃C₂T_z or (Ta_{0.05}Ti_{0.95})₃C₂T_z, and sonicated for 15 min. After adding EG (50 mL) to the above mixture, sonication was continued for 1 h. Then, the colloidal mixture was transferred to a three-necked round bottom flask and was purged with N₂. The mixture was refluxed at 160 °C for 2 h under N₂ environment with vigorous stirring. Upon cooling, the

product was washed several times with a water-ethanol mixture (20/80, v/v) and later with pure ethanol. As-synthesized MXene-Pt was dried in a desiccator overnight.

Material Characterization: X-ray diffraction (XRD) measurements were performed using a Bruker AXS D8 Advance with Cu-K α ($\lambda = 1.54 \text{ \AA}$) radiation. The scanning electron microscopy (SEM) analysis was acquired with Quanta 200 FEG ESEM coupled with an energy-dispersive X-ray spectroscopy detector (EDX-Genesis software) for elemental analysis. Transmission electron microscopy (TEM), and high resolution-TEM (HRTEM) analysis were performed using a JEOL JEM-2010F. X-ray photoelectron spectroscopy (XPS) measurements were performed using the 5600 Multi-Technique System (PHI, USA) in UHV (2.5×10^{-10} Torr base pressure). The samples were irradiated with an Al-K α monochromatic source (1486.6 eV) and the outcome electrons were analyzed by a spherical capacitor analyzer using the slit aperture of 0.8 mm. Spectra were shifted to adventitious C1s peak at 284.8 eV. Sputtering was done at a 6×6 mm raster with a rate of $16.7 \text{ \AA min}^{-1}$. CHN analysis was done using CHN-O analyzer, Flash 2000, Organic Elemental Analyzer. Raman measurements were performed using a HORIBA LabRAM HR Evolution Raman spectrometer with excitation laser lines of 532 nm.

Electrochemical Characterization: Potentiodynamic corrosion measurements were performed with a Biologic VSP 300 potentiostat in a three-electrode electrochemical cell (Pine) containing N₂ saturated 0.5 M H₂SO₄ at room temperature. A glassy carbon (GC, 0.197 cm²) rotating disc electrode (RDE), platinum mesh, and Ag/AgCl (sat. KCl) were used as working, counter, and reference electrodes, respectively. The GC disk was cleaned by polishing with diamond slurry followed by electrochemical cycling. Then, 20 μ L freshly prepared MXene colloid solution (0.2 g L⁻¹) was drop-casted on the GC surface and dried under vacuum. Loading of MXene on the electrode surface was 4 μ g. The electrochemical oxidation of MXene was monitored as a function of potential by performing an anodic scan from -0.2 versus OCP to 1.2 versus RHE. A scan rate of 0.167 mV s⁻¹, which was an American Society for Testing and Materials (ASTM) standard, was used. Before each scan, open circuit potential (OCP) was measured for 3 h to allow the system to equilibrate.

Mass change during electrochemical oxidation was measured with electrochemical crystal quartz microbalance (EQCM) using BluQCM QSD-300 (BioLogic). The working electrode was Au/Ti coated AT-cut quartz crystals with a 10 MHz nominal frequency and sensitivity of 0.0815 ng Hz⁻¹ cm² MXene (4 μ g) was loaded on the Au-coated surface. Platinum coil and Ag/AgCl (sat. KCl) was used as counter and reference electrode, respectively. The electrolyte was 0.5 M H₂SO₄.

Gas diffusion electrodes (GDEs) were fabricated using 5 cm² square carbon paper. Anodes were made using as-synthesized Pt-Ti₃C₂T_z and Pt-(Ta_{0.05}Ti_{0.95})₃C₂T_z catalysts, respectively. In brief, Nafion, water, and IPA were added with a volume ratio of 1:1:0.01 to the as-synthesized MXene-Pt in a vial and the mixture was sonicated for 30 min. Then, the homogeneously dispersed catalyst-ink was drop-cast on the microporous layer of the carbon paper and dried on a hot plate at 80 °C. For cathode side, blank carbon paper was used as one side of the NR-212 membrane was already coated with commercial Pt/C catalyst (one-sided NR-212, 0.3 mg Pt⁻¹ cm² Ion Power). The loading of Pt on all electrodes was 0.3 mg cm⁻². The membrane electrode assembly (MEA) was fabricated by hot-pressing the GDEs with NR-212 membrane electrolyte at 120 °C for 120 min at 0.5 MPa.

Fuel cell performances were tested in the Fuel Cell Testing System (850e, Scribner Associates Inc., North Carolina, USA) using a commercial single cell with a working area of 5 cm² PTFE gaskets (thickness: 230 μ m) were used at anode and cathode side to assemble the fuel cell. The fuel cell was operated at 80 °C with fully humidified H₂ (0.2 L min⁻¹) and O₂ (0.2 L min⁻¹) at the anode and cathode, respectively. Before each experiment, the cell was conditioned by a break-in procedure, consisting of 20 k cycles of alternating cell voltage between 0.6 V (5 min) and 0.35 V (5 min). After that, polarization curves were recorded from OCP to 0.3 V.

Accelerated stress tests (ASTs) were performed to evaluate the stability of as-synthesized MXene-Pt catalysts using a potentiostat (VSP-300, Bio-Logic). During AST, cell temperature was kept at 80 °C, and fully humidified H₂ and N₂ were supplied at anode and cathode, respectively. In this configuration, anode potential was used as the reference potential.

ASTs were done by performing 20 k cycles where each cycle consisted of holding potential at 0.6 V (3 s) and 0.9 V (3 s). The stability of catalysts was evaluated by comparing polarization curves after each 10 k cycles.

Computational Methods: All geometry optimizations and electronic properties were calculated using Density Functional Theory (DFT) for OK as implemented in the VASP package.^[54–57] The Perdew Burke-Ernzerhof (PBE) functional within the generalized gradient approximation (GGA) was applied to for the exchange-correlation.^[58–60] A Monkhorst-Pack Brillouin zone k-point sampling of $9 \times 9 \times 1$ was used for geometry optimization while a $11 \times 11 \times 1$ k-mesh was used for electronic properties analysis. A hexagonal Ti₃C₂ supercell of $2 \times 2 \times 1$ was used and a kinetic energy cut-off of 550 eV was applied in all calculations. The geometry optimization of atoms was performed by keeping convergence criteria for total energy and residual force up to 10^{-7} eV and 10^{-3} eV \AA^{-1} , respectively. A vacuum space of $\approx 8 \text{ \AA}$ in the perpendicular direction was employed along the z-direction to avoid interactions between two adjacent replicas in the z-direction. The Ti vacancy formation energy of Ti₃C₂ was calculated by the following expression:^[61]

$$E_F(\text{vacancy}) = E(\text{Ti}_3\text{C}_2 + \text{vacancy}) + E(\text{Ti}) - E(\text{Ti}_3\text{C}_2) \quad (9)$$

Here, $E(\text{Ti}_3\text{C}_2)$ was the total energy of the Ti₃C₂ supercell, $E(\text{Ti}_3\text{C}_2 + \text{vacancy})$ was the total energy of one Ti vacancy in the Ti₃C₂ supercell, while $E(\text{Ti})$ was the energy of most stable titanium bulk phase. The oxygen binding energy (OBE) on Ti₃C₂ surface was calculated by the following equation:^[62,63]

$$E(\text{OBE}) = E(\text{Ti}_3\text{C}_2 + \text{O}) - E(\text{Ti}_3\text{C}_2) - E(\text{O}_2) / 2 \quad (10)$$

where, $E(\text{Ti}_3\text{C}_2 + \text{O})$ and $E(\text{Ti}_3\text{C}_2)$ were the total energy of O adsorbed at Ti₃C₂ and the total energy of Ti₃C₂, while the single oxygen atom energy is considered as half of the O₂ molecule energy. Vesta software was utilized for visualization of optimized crystal structures. Additionally, the charge transfer amount after O adsorption on pristine has also been calculated and Ta-doped Ti₃C₂ surface by Bader charge analysis.^[64,65]

Supporting Information

Supporting Information is available from the Wiley Online Library or from the author.

Acknowledgements

B.F. and S.C. contributed equally to this work. The authors wish to acknowledge funding by the Deutsche Forschungsgemeinschaft (DFG) grant (EL 869/1-1 RA 659/30-1) through the German Research Foundation (DFG). Typographical errors in the Abstract and Figure 4 caption were corrected after initial online publication.

Conflict of Interest

The authors declare no conflict of interest.

Data Availability Statement

The data that support the findings of this study are available in the supplementary material of this article.

Keywords

corrosion, durability, DFT, fuel cells, MXene

Received: August 16, 2023

Revised: October 17, 2023

Published online: November 3, 2023

- [1] Y. Wang, D. F. Ruiz Diaz, K. S. Chen, Z. Wang, X. C. Adroher, *Mater. Today*. **2020**, *32*, 178.
- [2] Y. Liu, T. G. Kelly, J. G. Chen, W. E. Mustain, *ACS Catal.* **2013**, *3*, 1184.
- [3] E. R. Hamo, B. A. Rosen, *Nano Res.* **2022**, *15*, 10218.
- [4] J. D. Sinniah, W. Y. Wong, K. S. Loh, R. M. Yunus, S. N. Timmiati, *J. Power Sources*. **2022**, *534*, 231422.
- [5] C. B. Krishnamurthy, O. Lori, L. Elbaz, I. Grinberg, *J. Phys. Chem. Lett.* **2018**, *9*, 2229.
- [6] Z. Li, L. Yu, C. Milligan, T. Ma, L. Zhou, Y. Cui, Z. Qi, N. Libretto, B. Xu, J. Luo, E. Shi, Z. Wu, H. Xin, W. N. Delgass, J. T. Miller, Y. Wu, *Nat. Commun.* **2018**, *9*, 5258.
- [7] W. Kong, J. Deng, L. Li, *J. Mater. Chem. A*. **2022**, *10*, 14674.
- [8] A. Liu, X. Liang, X. Ren, W. Guan, M. Gao, Y. Yang, Q. Yang, L. Gao, Y. Li, T. Ma, *Adv. Funct. Mater.* **2020**, *30*, 2003437.
- [9] M. Naguib, V. N. Mochalin, M. W. Barsoum, Y. Gogotsi, *Advanced Materials*. **2014**, *26*, 1005.
- [10] L. Verger, V. Natu, M. Carey, M. W. Barsoum, *Trends in chemistry*. **2019**, *1*, 656.
- [11] S. G. Peera, C. Liu, A. K. Sahu, M. Selvaraj, M. C. Rao, T. G. Lee, R. Koutavarapu, J. Shim, L. Singh, *Adv. Mater. Interfaces*. **2021**, *8*, 2100975.
- [12] N. H. Ahmad Junaidi, W. Y. Wong, K. S. Loh, S. Rahman, W. R. W. Daud, *Int. J. Energy Res.* **2021**, *45*, 15760.
- [13] C. Xu, *ACS Appl. Mater. Interfaces*. **2020**, *12*, 19539.
- [14] X. Xie, S. Chen, W. Ding, Y. Nie, Z. Wei, *Chem. Commun.* **2013**, *49*, 10112.
- [15] A. Iqbal, J. Hong, T. Y. Ko, C. M. Koo, *Nano Convergence*. **2021**, *8*, 9.
- [16] T. Habib, X. Zhao, S. A. Shah, Y. Chen, W. Sun, H. An, J. L. Lutkenhaus, M. Radovic, M. J. Green, *npj 2D Materials and Applications*. **2019**, *3*, 8.
- [17] C. J. Zhang, S. Pinilla, N. Mcevoy, C. P. Cullen, B. Anasori, E. Long, S.-H. Park, A. Seral-Ascaso, A. Shmeliov, D. Krishnan, C. Morant, X. Liu, G. S. Duesberg, Y. Gogotsi, V. Nicolosi, *Chem. Mater.* **2017**, *29*, 4848.
- [18] J. Halim, K. M. Cook, M. Naguib, P. Ekland, Y. Gogotsi, J. Rosen, M. W. Barsoum, *Appl. Surf. Sci.* **2016**, *362*, 406.
- [19] V. Natu, J. L. Hart, M. Sokol, H. Chiang, M. L. Taheri, M. W. Barsoum, *Angew. Chem.* **2019**, *131*, 12785.
- [20] H. Liang, J. Liu, *Chem. Cat. Chem.* **2022**, *14*, e202101375.
- [21] C. Tsounis, P. V. Kumar, H. Masood, R. P. Kulkarni, G. S. Gautam, C. R. Müller, R. Amal, D. A. Kuznetsov, *Angew. Chem., Int. Ed.* **2023**, *62*, e202210828.
- [22] D. Göhl, H. Rueß, M. Pander, A. R. Zerardjanin, K. J. J. Mayrhofer, J. M. Schneider, A. Erbe, M. Ledendecker, *J. Electrochem. Soc.* **2020**, *167*, 021501.
- [23] W. Yuan, *ACS Sustainable Chem. Eng.* **2018**, *6*, 8976.
- [24] Y. Jiang, T. Sun, X. Xie, W. Jiang, J. Li, B. Tian, C. Su, *ChemSusChem*. **2019**, *12*, 1368.
- [25] T. A. Le, *ACS Sustainable Chem. Eng.* **2019**, *7*, 16879.
- [26] M. Han, J. Yang, J. Jiang, R. Jing, S. Ren, C. Yan, *J. Colloid Interface Sci.* **2021**, *582*, 1099.
- [27] N. Shpigel, F. Malchik, M. D. Levi, B. Gavriel, G. Bergman, S. Tirosh, N. Leifer, G. Goobes, R. Cohen, M. Weitman, H. Aviv, Y. R. Tischler, D. Aurbach, Y. Gogotsi, *Energy Storage Mater.* **2020**, *32*, 1.
- [28] J. Tang, T. S. Mathis, N. Kurra, A. Sarycheva, X. X. Xiao, M. N. Hedhili, Q. Jiang, H. N. Alshareef, B. Xu, F. Pan, Y. Gogotsi, *Angew. Chem.* **2019**, *131*, 18013.
- [29] E. R. Hamo, P. Tereshchuk, M. Zysler, D. Zitoun, A. Natan, B. A. Rosen, *J. Electrochem. Soc.* **2019**, *166*, F1292.
- [30] E. R. Hamo, R. K. Singh, J. C. Douglin, S. Chen, M. B. Hassine, E. Carbo-Argibay, S. Lu, H. Wang, P. J. Ferreira, B. A. Rosen, D. R. Dekel, *ACS Catal.* **2021**, *11*, 932.
- [31] V. Natu, R. Pai, O. Wilson, E. Gadasu, H. Badr, A. Karmakar, A. J. D. Magenau, V. Kalra, M. W. Barsoum, *Chem. Mater.* **2022**, *34*, 678.
- [32] I. Persson, J. Halim, T. W. Hansen, J. B. Wagner, V. Darakchieva, J. Palisaitis, J. Rosen, P. O. Å. Persson, *Adv. Funct. Mater.* **2020**, *30*, 1909005.
- [33] P. Nayak, R. C. Xie, R. G. Palgrave, R. G. Compton, *Chem. Electro. Chem.* **2021**, *8*, 911.
- [34] O. Mashtalir, M. Naguib, V. N. Mochalin, Y. Dall'agnese, M. Heon, M. W. Barsoum, Y. Gogotsi, *Nat. Commun.* **2013**, *4*, 1716.
- [35] M. T. P. Rigby-Bell, V. Natu, M. Sokol, D. J. Kelly, D. G. Hopkinson, Y. Zou, J. R. T. Bird, L. J. Evitts, M. Smith, C. P. Race, P. Frankel, S. J. Haigh, M. W. Barsoum, *RSC Advances*. **2021**, *11*, 3114.
- [36] P. Tereshchuk, D. Golodnitsky, A. Natan, *J. Phys. Chem. C*. **2020**, *124*, 7716.
- [37] P. Shang, S. Xiong, L. Li, D. Tian, W. Ai, *Appl. Surf. Sci.* **2013**, *285*, 713.
- [38] T. Grewe, H. Tüysüz, *Chem. Nano. Mat.* **2016**, *2*, 273.
- [39] K. J. Meisner, R. Zaman, B.-C. Zhou, *Calphad*. **2022**, *76*, 102391.
- [40] E. Gebhardt, *ii. Reactions and equilibria between mixed crystals and oxide phases*. **1959**, *50*.
- [41] A. Jain, S. P. Ong, G. Hautier, W. Chen, W. D. Richards, S. Dacek, S. Cholia, D. Gunter, D. Skinner, G. Ceder, K. A. Persson, *APL Mater.* **2013**, *1*, 011002.
- [42] I. P. Zibro, V. P. Filonenko, E. E. Nikishina, E. N. Lebedeva, D. V. Drobot, *Inorg. Mater.* **2016**, *52*, 38.
- [43] I. P. Zibrov, V. P. Filonenko, M. V. Trenikhin, E. E. Nikishina, E. N. Lebedeva, D. V. Drobot, *Inorg. Mater.* **2019**, *55*, 489.
- [44] I. P. Zibrov, V. P. Filonenko, N. D. Zakharov, P. Werner, D. V. Drobot, E. E. Nikishina, E. N. Lebedeva, *J. Solid State Chem.* **2013**, *203*, 240.
- [45] R. Bassiri, F. Liou, M. R. Abernathy, A. C. Lin, N. Kim, A. Mehta, B. Shyam, R. L. Byer, E. K. Gustafson, M. Hart, I. Maclaren, I. W. Martin, R. K. Route, S. Rowan, J. F. Stebbins, M. M. Fejer, *APL Mater.* **2015**, *3*, 036103.
- [46] C. Taviot-Gueho, J. Cellier, A. Bousquet, E. Tomasella, *J. Phys. Chem. C*. **2015**, *119*, 23559.
- [47] E. E. Nikishina, E. N. Lebedeva, D. V. Drobot, *Inorg. Mater.* **2012**, *48*, 1243.
- [48] G. L. W. Hart, R. W. Forcade, *Phys. Rev. B*. **2009**, *80*, 014120.
- [49] F. Cao, *Adv. Mat.* **2022**, *34*, 2107554.
- [50] F. Bu, M. M. Zagho, Y. Ibrahim, B. Ma, A. Elzatahry, D. Zhao, *Nano Today*. **2020**, *30*, 100803.
- [51] Z. Wu, Y. Deng, J. Yu, J. Han, T. Shang, D. Chen, N. Wang, S. Gu, W. Lv, F. Kang, Y. Tao, Q.-H. Yang, *Adv. Mater.* **2023**, *35*, 2300580.
- [52] S. Hong, J. K. El-Demellawi, Y. Lei, Z. Liu, F. A. Marzooqi, H. A. Arafat, H. N. Alshareef, *ACS Nano*. **2022**, *16*, 792.
- [53] T. Ioroi, K. Yasuda, *J. Power Sources*. **2020**, *450*, 227656.
- [54] G. Kresse, J. Hafner, *Phys. Rev. B*. **1993**, *47*, 558.
- [55] G. Kresse, J. Hafner, *Phys. Rev. B*. **1994**, *49*, 14251.
- [56] G. Kresse, J. Furthmüller, *Comput. Mater. Sci.* **1996**, *6*, 15.
- [57] G. Kresse, J. Furthmüller, *Phys. Rev. B*. **1996**, *54*, 11169.
- [58] J. P. Perdew, K. Burke, M. Ernzerhof, *Physical review letters*. **1996**, *77*, 3865.
- [59] J. P. Perdew, K. Burke, M. Ernzerhof, *Phys. Rev. Lett.* **1996**, *78*, 1396.
- [60] J. Paier, R. Hirschl, M. Marsman, G. Kresse, *J. Chem. Phys.* **2005**, *122*, 234102.
- [61] S. Thomas, A. Zaeem, *Advanced Theory and Simulations*. **2021**, *4*, 2000250.
- [62] V. Kumar, D. Azhikodan, D. R. Roy, *J. Hazard. Mater.* **2021**, *405*, 124168.
- [63] V. Kumar, A. Bano, D. R. Roy, *ACS Appl. Nano Mater.* **2021**, *4*, 2440.
- [64] W. Orville-Thomas, *Atoms in Molecules—a Quantum Theory*, Clarendon press, Oxford, UK **1996**, p. 438.
- [65] G. Henkelman, A. Arnaldsson, H. Jónsson, *Comput. Mater. Sci.* **2006**, *36*, 354.